

REPORT DOCUMENTATION PAGE

Public reporting burden for this collection of information is estimated to average 1 hour per response, including the time for reviewing the data needed, and completing and reviewing this collection of information. Send comments regarding this burden estimate reducing this burden to Washington Headquarters Services, Directorate for Information Operations and Reports, 1215 Jefferson Management and Budget, Paperwork Reduction Project (0704-0188), Washington, DC 20503

01876

ing
r
of

1. AGENCY USE ONLY (Leave blank)		2. REPORT DATE 31-12-2004	3. REPORT TYPE AND DATES COVERED Final 10/01 - 9/04	
4. TITLE AND SUBTITLE Blade Row Interaction Unsteady Aerodynamics & Variability for Aeromechanics and HCF			5. FUNDING NUMBERS F49620-02-1-0040	
6. AUTHOR(S) Sanford Fleeter				
7. PERFORMING ORGANIZATION NAME(S) AND ADDRESS(ES) Purdue Research Foundation 1063 Hovde Hall West Lafayette, IN 47907-1063			8. PERFORMING ORGANIZATION REPORT NUMBER	
9. SPONSORING / MONITORING AGENCY NAME(S) AND ADDRESS(ES) AFOSR/NA 4015 Wilson Blvd. Room 713 Arlington, VA 22203-1954			10. SPONSORING / MONITORING AGENCY REPORT NUMBER	
11. SUPPLEMENTARY NOTES				
12a. DISTRIBUTION / AVAILABILITY STATEMENT Distribution Statement A. Approved for public release; distribution is unlimited.			12b. DISTRIBUTION CODE	
13. ABSTRACT (Maximum 200 Words) This research is directed at the development of the technology needed to accurately predict significant blade row forced response in a multistage environment. Specific objectives include addressing design and off-design blade row interaction unsteady aerodynamics including unsteady aerodynamic variability. The technical approach requires that blade row interaction unsteady aerodynamic data be acquired and analyzed for realistic geometries and flow conditions. Thus, experiments are performed in the Purdue Transonic Research Compressor Facility. It features a 1-1/2 stage axial-flow geometry representative of that used in the front stages of advanced high-pressure compressors including advanced controlled diffusion airfoil (CDA) designed in cooperation with Pratt & Whitney. Note that this compressor design was directed at transonic blade row interaction unsteady aerodynamics and HCF studies.				
14. SUBJECT TERMS Unsteady Aerodynamics, Aeromechanics, Turbomachinery, Forced Response			15. NUMBER OF PAGES 20	
			16. PRICE CODE	
17. SECURITY CLASSIFICATION OF REPORT UNCLASSIFIED	18. SECURITY CLASSIFICATION OF THIS PAGE UNCLASSIFIED	19. SECURITY CLASSIFICATION OF ABSTRACT UNCLASSIFIED	20. LIMITATION OF ABSTRACT	

20050519 096

INTRODUCTION

Compressor designs featuring higher tip speeds, increased steady loading, and fewer stages of closely spaced rows of low-aspect ratio thin airfoils have enabled the development of advanced aircraft engines with increased thrust-to-weight ratio and reduced fuel consumption. Unfortunately, these blade rows are highly susceptible to flow-induced vibrations and high cycle fatigue (HCF). In fact, the loss of blades, vanes, and disks due to HCF is currently the predominant surprise engine failure mode in the field. The driving phenomenon for these flow-induced vibrations is the blade row interaction unsteady aerodynamics, with transonic compressors of particular interest. Specifically, a transonic rotor generates shocks that propagate upstream and wakes that convect downstream. The shocks are thus a forcing function to upstream vane rows, with wakes an unsteady forcing function to downstream stator rows.

To avoid surprise HCF failures, accurate vibratory stress predictions are crucial. This requires validated design systems appropriate for multi-stage blade rows at both design and off-design conditions. Time-accurate multi-blade row CFD analyses are now beginning to be utilized to analyze blade row interactions in advanced turbomachine designs. Although these analyses account for blade row interactions, the computational domain is typically reduced by scaling the geometry such that each airfoil row is represented by a single passage or a very few passages at most. This greatly reduces computer processing time and storage requirements, but alters the fundamental periodicity of the blade row interactions, i.e. the interblade phase angle specified by the blade-vane count ratio. In addition, these analyses are generally applied at the design condition, with off-design conditions analyzed only after an HCF problem is found. In fact, minimal if any predictions of the unsteady aerodynamics of multistage blade rows at off-design conditions have been made. Fundamental blade row interaction data are thus needed to assess the validity of these time-accurate multi-blade row CFD analyses, with these data obtained for realistic modern airfoil designs at high-speed design and off-design conditions.

RESEARCH OBJECTIVES & TECHNICAL APPROACH

The overall objective of this research was to develop technology needed to accurately predict significant blade row forced response in a multistage environment. Specific objectives include addressing design and off-design blade row interaction unsteady aerodynamics including unsteady aerodynamic variability.

The technical approach requires that blade row interaction unsteady aerodynamic data be acquired and analyzed for realistic geometries and flow conditions. Thus, experiments are performed in the Purdue Transonic Research Compressor Facility. It features a 1-½ stage axial-flow geometry representative of that used in the front stages of advanced high-pressure compressors including advanced controlled diffusion airfoil (CDA) designed in cooperation with Pratt & Whitney. Note that this compressor design was directed at transonic blade row interaction unsteady aerodynamics and HCF studies.

DISTRIBUTION STATEMENT A
Approved for Public Release
Distribution Unlimited

RESEARCH TRANSONIC COMPRESSOR

The Purdue Transonic Research Compressor features a 1½-stage axial-flow geometry representative of the front stages of modern aircraft high-pressure compressors. Air is drawn into the test section through a bell-mouth inlet (16:1 contraction ratio), with the compressor mass flow rate regulated by a butterfly throttle valve. Power is provided by a 400 horsepower motor and transmitted to the rotor through a variable speed magnetic clutch and an 8:1 ratio gearbox. The compressor test section includes an IGV and stator ring with variable stagger vanes. The IGV ring can be circumferentially indexed relative to stationary instrumentation or the downstream stator to investigate the effect of vane clocking on compressor performance. Spacer assemblies within the test section permit the IGV-rotor and rotor-stator axial spacing to be varied, allowing the forcing function decay rate and resulting vane response to be characterized.

The compressor has a 12.0 in. tip diameter, 0.67 hub-to-tip ratio. The baseline configuration consists of 18 inlet guide vanes (IGVs), 19 rotor blades, and 18 downstream stators. Both the inlet guide and stator vane possess an advanced controlled diffusion airfoil (CDA) profile with a constant 7% thickness and 1.75 in. chord. This baseline rotor consists of airfoils possessing a NACA 65 series profile on circular arc meanlines, 2.0 in. chord, and a thickness distribution tapering from 10% chord at the root to 6% at the tip. The compressor was reconfigured with 20 IGVs and stators, and an advanced-design high-speed rotor designed in conjunction with Pratt & Whitney, Figure 1. This integrally bladed disk contains 18 controlled diffusion airfoils with a 2.0 in. chord and a thickness distribution varying linearly from 8% chord at the root to 4% at the tip.

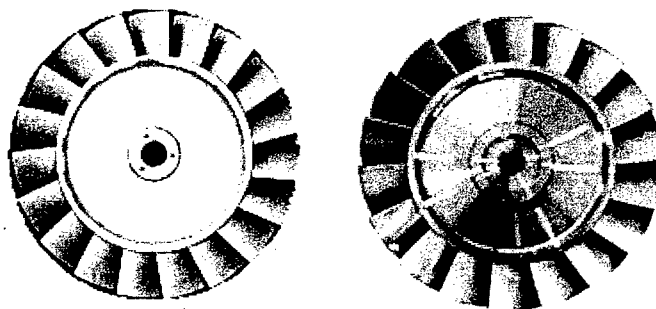


Figure 1. Baseline and advanced-design rotors

Unsteady Aerodynamic Instrumentation

Measurements of the rotor generated unsteady aerodynamic forcing function and the resultant IGV steady and unsteady surface pressure distributions are made at 90% span. An unsteady static pressure probe is used to measure the potential flow generated forcing function upstream of the rotor, with vane mounted high-response Kulite pressure transducers used to measure the resultant IGV unsteady surface pressure response. These transducers are reverse mounted within the suction surface of one vane and the pressure surface of an adjacent vane. To minimize probe interference effects, the unsteady static pressure probe is located 21.4% vane chord downstream of the IGV trailing edge and circumferentially positioned at 44.55% pitch between the trailing edges of the vanes adjacent to the instrumented passage.

Measurements of the rotor wake generated unsteady aerodynamic forcing function to the downstream stator and the resultant stator steady and unsteady surface pressure distributions are made at 50% and 90% span. Miniature probes designed to access the confined regions between the blade rows are utilized to make these inter-stage measurements at the stator inlet. These probes include a five hole prism probe, a conventional total temperature probe, an unsteady static pressure probe, and a cross hot-film anemometer probe.

Particle Image Velocimetry (PIV)

The DANTEC PIV system utilized consists of a 30 mJ Nd:YAG laser with twin oscillators, a high-resolution digital camera operated in the cross-correlation mode, and a PC-controlled PIV-2100 Processor. This processor also synchronizes the camera and laser, and is capable of resolving the particle displacement to within 1/10 of a pixel through the use of sub-pixel interpolation schemes. A thermal aerosol generator is used that produces a high volume of particles by discharging a heated and pressurized glycol based mixture into the atmosphere where it immediately vaporizes and then condenses into a fine mist of monodisperse particles. A uniform test section seeding density is achieved by introducing these particles upstream of the inlet and allowing them to disperse into the ambient air prior to being drawn through the facility.

The vane-to-vane flow field is illuminated by a 1 mm thick light sheet introduced upstream through the bellmouth inlet using a combination of cylindrical and spherical lenses and downstream of the stator through an optical probe. The instantaneous vane-to-vane flows are measured for several time instants over one rotor blade-passing period. A once-per-revolution pulse from a photo-optic sensor on the shaft triggers the PIV 2100 Processor that then fires the lasers and records the camera CCD images. To record images at different points over one interaction cycle, the rotor speed is used to calculate the time delay to position the rotor at the desired angular location relative to the stationary vanes.

RESULTS

Off-Design Rotor-IGV Interactions

A transonic rotor operates with a supersonic relative velocity and a subsonic absolute velocity. Shocks thus form near the rotor blade leading edges that propagate into an upstream vane row. Since compressors operate over a range of inlet conditions, the corrected and mechanical conditions can differ significantly for different missions. Also, since the variable inlet vane stagger reset is determined by the corrected rotor speed, the specific inlet vane stagger angle at the resonant mechanical speed can vary considerably depending on compressor inlet conditions. The majority of blade row interaction resonance issues are at off-design operating conditions where the incidence differs considerably from those near peak efficiency.

The forcing function to the upstream vane row is the modal force on the vanes, determined by integrating the in-phase components of the vane surface unsteady pressures and the vibratory displacement. Since the rotor leading edge shocks for transonic flow and the rotor potential field for subsonic flow generate the unsteady pressure loading on the upstream inlet vanes, the modal force driving the vibratory response is strongly dependent on the rotor inlet conditions set by the corrected speed. In fact, the highest inlet vane strains might be expected when the rotor inlet vane reset causes the rotor to just be on the verge of becoming transonic and the IGV trailing edge metal angle is aligned with the detached rotor shocks, Figure 2. The rotor

shocks then "slap" the upstream vanes. Mathematically the forcing function is in-phase with vibratory modes having constant spatial phase such as first bending, resulting in the maximum possible modal force excitation for these modes.

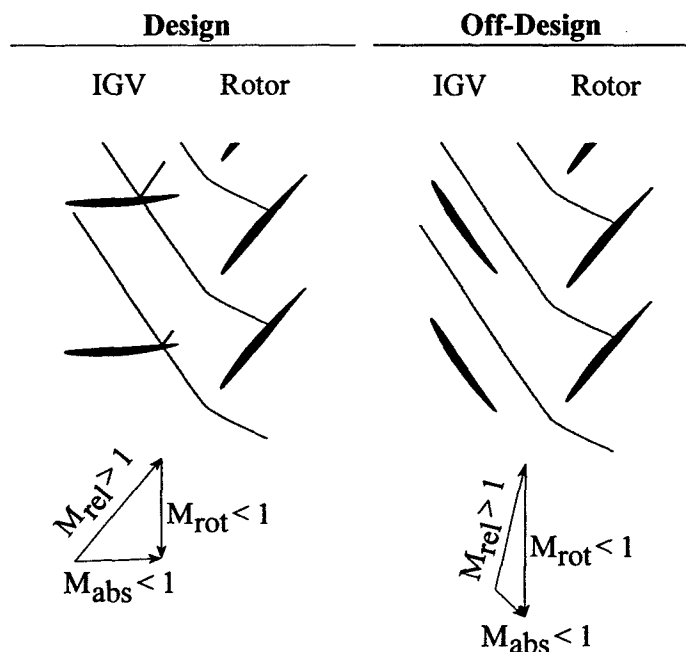


Figure 2. Rotor-IGV interactions

Rotor-Generated Forcing Function

The rotor-generated unsteady static pressure field data is presented in Figure 3. The static pressure perturbation is non-dimensionalized by the inlet total pressure, time non-dimensionalized by blade-pass period, and only five of the nineteen blade-pass periods in a revolution are shown.

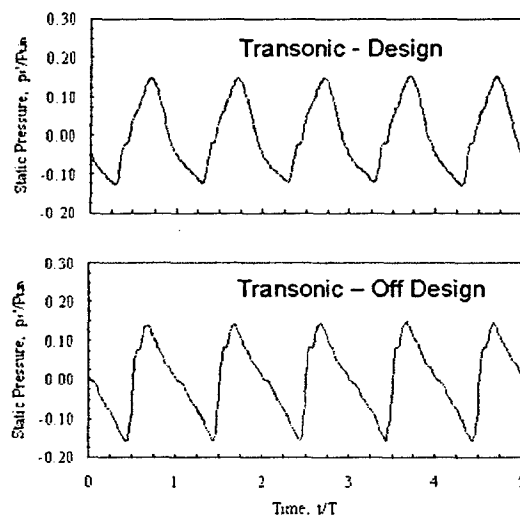


Figure 3. Rotor generated forcing function to IGVs

The static pressure fluctuations at the subsonic operating condition are essentially sinusoidal, reaching a maximum $p_s/P_{t,in}$ value of 0.15. At the off-design condition, the rotor relative velocity is transonic, demonstrated by the impulsive static pressure rise corresponding to the passing of rotor leading edge shocks. This impulsive peak-to-peak amplitude is only slightly larger than that at design.

IGV Unsteady Aerodynamic Response

IGV unsteady pressure envelopes, the minimum and maximum unsteady pressures in the time-variant IGV response at each chordwise location, are presented together with the respective time-average surface pressure distributions in Figure 4.

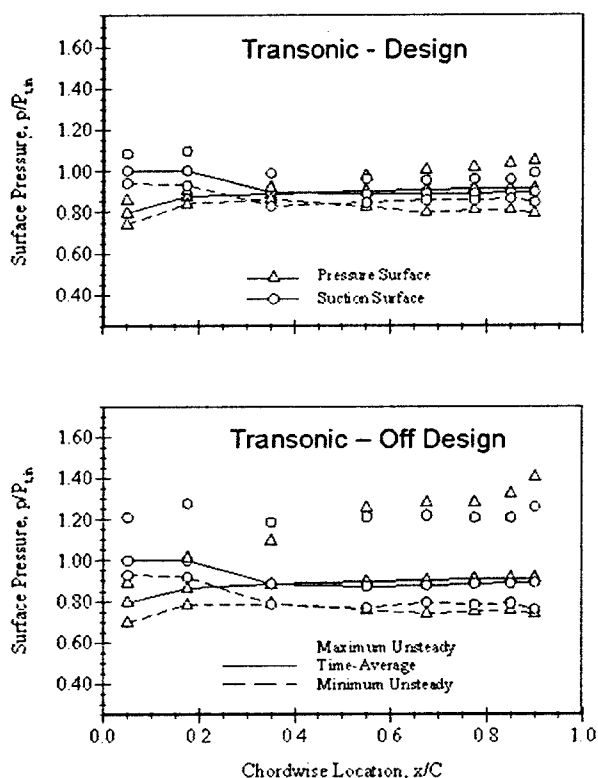


Figure 4. IGV unsteady pressure envelopes

The time-average pressure distributions indicate a high pressure region associated with the presence of a stagnation point on the IGV suction surface at both operating conditions. The pressure surface data reveal a low pressure area at the leading edge that decreases as the corrected speed is increased.

The unsteady surface pressure amplitudes are smallest at design. After reaching a maximum at 17.5% chord, the suction surface unsteadiness decreases smoothly to approximately 10% $P_{t,in}$ near 65% chord. Over the remainder of the surface, the unsteadiness is relatively constant except near the trailing edge where the pressure fluctuations are nearly equal to those at the leading edge. The vane pressure surface unsteadiness decreases over the leading 35% chord, with the unsteady pressure envelope increasing significantly to a maximum of 25.3% $P_{t,in}$ near the trailing edge.

The IGV response to the rotor leading edge shocks at off-design is dramatic, with unsteady loading greater than 40% of the inlet total pressure over the majority of both vane surfaces. The suction surface envelope increases between the leading edge and 35% chord, with the static pressure fluctuations then remaining relatively constant. An increase in the trailing edge region, similar to that at design, raises the unsteadiness to almost 50% of the inlet total pressure. In contrast, the pressure surface unsteadiness sharply rises near the leading edge to 55% chord and continues to increase to a maximum of 66% $P_{t,in}$ in the trailing edge region. This maximum, while occurring at the same location, is 2.6 times larger than that at design, with the forcing function peak-to-peak static pressure perturbation only 1.1 times larger.

Time-Variant Surface Pressures

IGV surface pressures at several time instances provide insight into the upstream propagating wave phenomena. The surface pressures are presented for ten equally spaced time increments over one rotor blade-pass period along with the rotor generated unsteady static pressure field. Recall the forcing function data were not shifted to the reference vane trailing edge and therefore lag the surface pressure measurements by 43.3% of a blade-pass period. For reference, symbols on the forcing function correspond to the time at which the surface pressure data are acquired.

An upstream propagating wave phenomenon is evident in the time-variant pressure distributions at design as the IGVs smoothly respond to the unsteady rotor generated potential field, Figure 5. The pressure surface trailing edge static pressure gradually increases between $t/T=0.8 - 0.3$. This static pressure peak migrates toward the leading edge as the interaction cycle progresses. The suction surface fluctuations are small aft of mid-chord, with leading edge region unsteadiness dominate over the cycle.

The time-variant pressure data for the transonic off-design operating condition, Figure 6, also indicate an upstream propagating phenomenon. A response is first observed on the pressure surface trailing edge at $t/T=0.2$. This significant static pressure rise results from the impact of a rotor leading edge shock and the subsequent reflection generated at the vane surface. Note a time lag exists between the forcing function and vane response because the trailing edge unsteady pressure tap is 32% chord upstream of the unsteady static pressure probe.

At $t/T=0.3$, the shock and reflection have progressed upstream, with a sharp static pressure decrease aft of a maximum value of 130% $P_{t,in}$ at 85% chord. The suction surface static pressure rise indicates that the incident shock has diffracted around the trailing edge at $t/T=0.4$. The suction surface trailing edge unsteadiness is approximately equal to the maximum pressure surface fluctuation which has migrated upstream to 67.5% chord. A noticeable pressure surface unsteadiness decrease occurs at the next time instant, with higher suction surface static pressures over the majority of the chord. The suction surface unsteadiness grows as it travels toward the leading edge, reaching a maximum at $t/T=0.0$. Pressure surface fluctuations are minimal at these later times, a result of decreased shock strength as energy is dissipated during its interaction with the upstream vane row. Additionally, the pressure and suction surface trailing edge pressure distributions are nearly identical for the remainder of the cycle up to $t/T=0.1$.

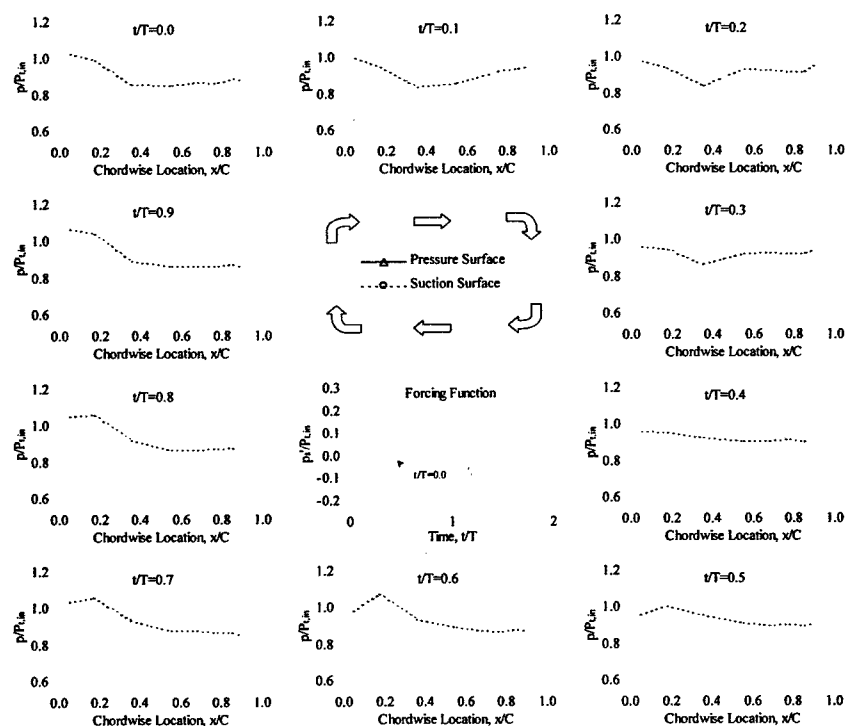


Figure 5. Time-variant IGV loading – transonic design

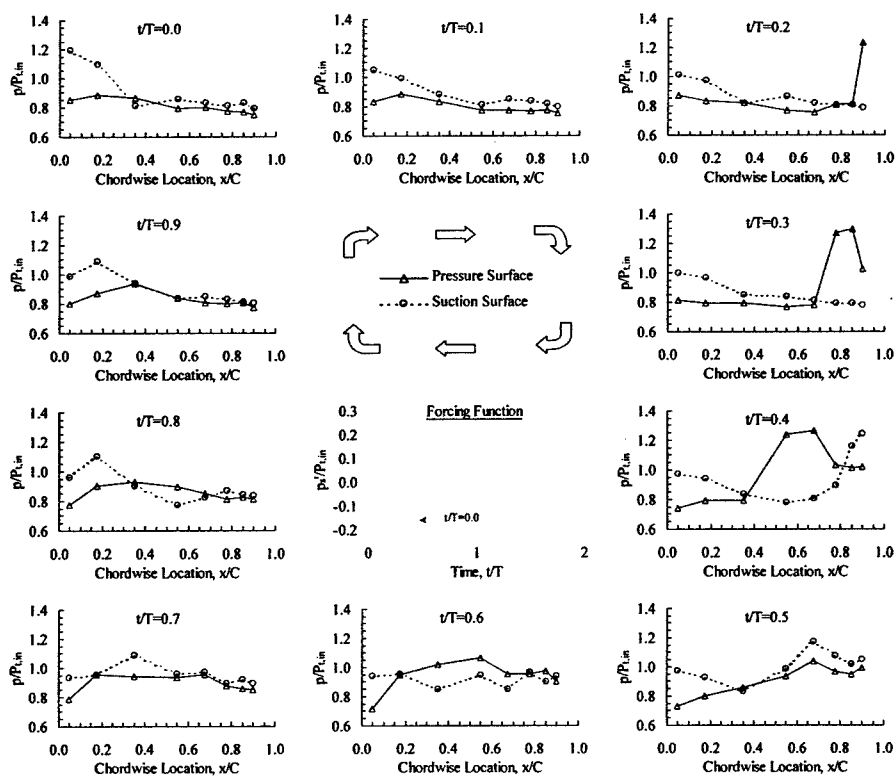


Figure 6. Time-variant IGV loading – transonic off-design

IGV-to-IGV Passage Flow Field

PIV measurements of the unsteady vane-to-vane flow field at 90% span are obtained at ten equally spaced time intervals over one blade-pass period, with the data at each time instant representing an ensemble average of 32 instantaneous vector fields. Complex rotor-IGV interactions are revealed in the time-variant absolute Mach number results for the transonic operating condition, Figure 7.

A rotor leading edge shock is first cut by the upper vane pressure surface and diffracted around the trailing edge at $t/T=0.2$, with the diffracted shock segment clearly evident on the suction surface at the next time instant. This shock weakens slightly as it progresses upstream, moving closer to the lower vane pressure surface. At $t/T=0.6$, a process has begun which splits the shock into two segments near mid-passage 0.3 blade-pass periods later. The weaker of the two segments decays rapidly, while the remaining shock segment continues toward the lower vane pressure surface. This segment impacts the pressure surface between $t/T=0.1$ and $t/T=0.2$ and a resultant reflection from the surface forms as indicated by the low velocity region behind the shock. As the shock and reflection travel upstream, the high velocity region ahead of the shock merges with a leading edge high velocity region of nearly equal magnitude at $t/T=0.3$. This high velocity region decays with time, encompassing a majority of the leading edge to $t/T=0.6$ and reaching a minimum at $t/T=0.0$. As this high velocity region weakens, a corresponding low velocity region grows on the pressure surface leading edge, and vice versa, throughout the rotor-IGV interaction cycle.

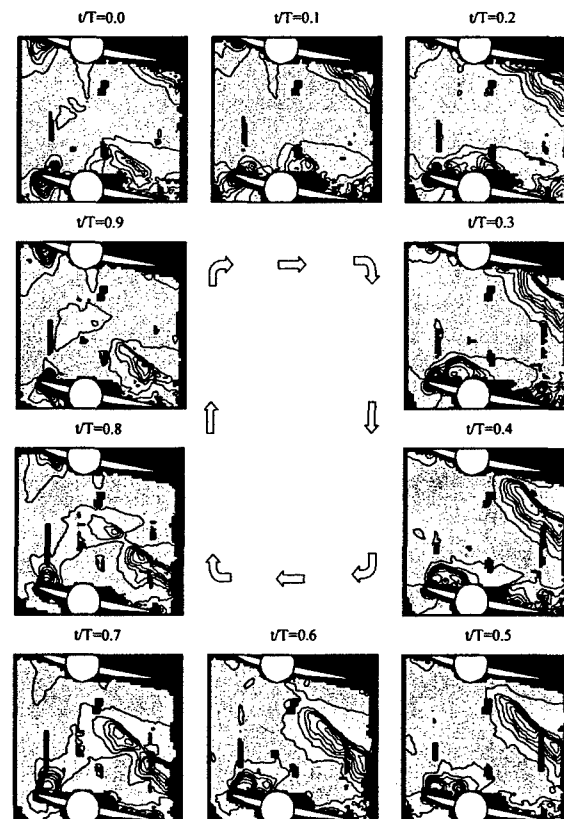


Figure 7. Time-variant IGV absolute Mach number – transonic off-design

A rotor leading edge shock is first cut by the upper vane pressure surface and diffracted around the trailing edge at $t/T=0.2$, with the diffracted shock segment clearly evident on the suction surface at the next time instant. This shock weakens slightly as it progresses upstream, moving closer to the lower vane pressure surface. At $t/T=0.6$, a process has begun which splits the shock into two segments near mid-passage 0.3 blade-pass periods later. The weaker of the two segments decays rapidly, while the remaining shock segment continues toward the lower vane pressure surface. This segment impacts the pressure surface between $t/T=0.1$ and $t/T=0.2$ and a resultant reflection from the surface forms as indicated by the low velocity region behind the shock. As the shock and reflection travel upstream, the high velocity region ahead of the shock merges with a leading edge high velocity region of nearly equal magnitude at $t/T=0.3$. This high velocity region decays with time, encompassing a majority of the leading edge to $t/T=0.6$ and reaching a minimum at $t/T=0.0$. As this high velocity region weakens, a corresponding low velocity region grows on the pressure surface leading edge, and vice versa, throughout the rotor-IGV interaction cycle.

The spatial periodicity of the unsteady flow field is also demonstrated, with this periodicity set by the unequal blade-vane count. This is best illustrated at $t/T=0.0$ where two shock segments are visible in the passage; one near the lower vane pressure surface and the other just below the upper vane trailing edge. The data correctly show the circumferential distance between adjacent rotor leading edge shocks is slightly smaller than that of the IGVs, a consequence of the compressor having 18 IGVs and 19 rotor blades. Thus, interactions on the upper vane lead those on the lower vane by an interblade phase of 380° , with any given rotor blade requiring 1.06 blade-pass periods to traverse an IGV passage.

CDA Rotor Generated Unsteady Aerodynamics of an Upstream Vane

Experiments were performed in an advanced design multistage axial-flow compressor that incorporates Controlled Diffusion Airfoils (CDA) to investigate IGV-rotor unsteady aerodynamic blade row interaction phenomena. The focus of this research was on transonic operation near the tip region of the blading. This work provides a follow on to earlier studies that used CDA airfoil sections on the stationary vanes and a NACA 65 section rotor.

Rotor Generated Forcing Function

For comparison purposes, the effect of steady compressor loading on the rotor generated unsteady static pressure field, i.e., the forcing function to the upstream IGV, is shown in Figure 8 for both the original NACA 65 bladed rotor and the CDA bladed rotor. Presented is the time-variant static pressure nondimensionalized by the time-average inlet total pressure, with time nondimensionalized by the blade pass period. For the NACA-65 transonic case (20,000 rpm), the data show a significant perturbation magnitude of 30% of the inlet total pressure. The sharp compression is due to the strong normal shock that is produced by these airfoils.

The CDA airfoils show both a significant change in character and magnitude when compared to the NACA rotor. In terms of magnitude, the reduction ranges from a factor of 3 to 4 depending on the loading case. The character of the waveform also changes considerably from low to high loading.

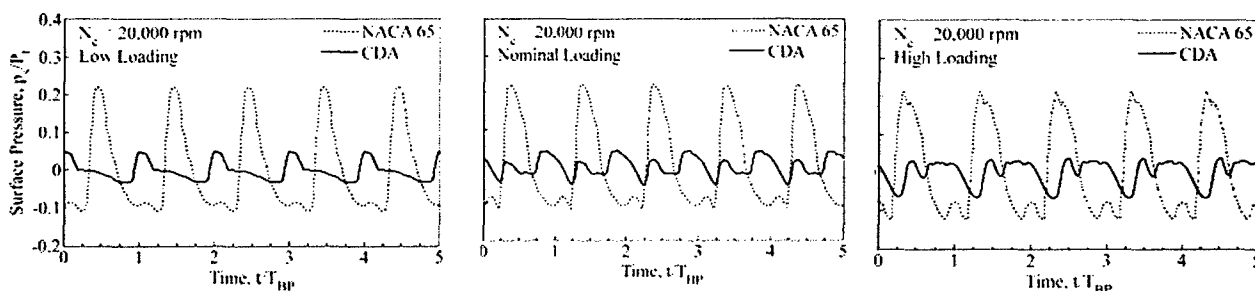


Figure 8. Transonic rotor-generated forcing function

The unsteadiness on the IGV surfaces is shown in Figures 9 and 10 as vane surface unsteady pressure envelopes. For comparison purposes, the envelopes measured when the rig featured the NACA 65 rotor are also shown. The NACA 65 data is at the nominal loading point, but the IGV loading is very low at this 90% span location and there is little variation of the forcing function with loading. Thus, these data are valid for a comparison benchmark for all loading conditions with the CDA rotor. The shaded region within the solid lines represents the response envelopes with the CDA rotor generated forcing function, and the dashed lines that with the NACA forcing function.

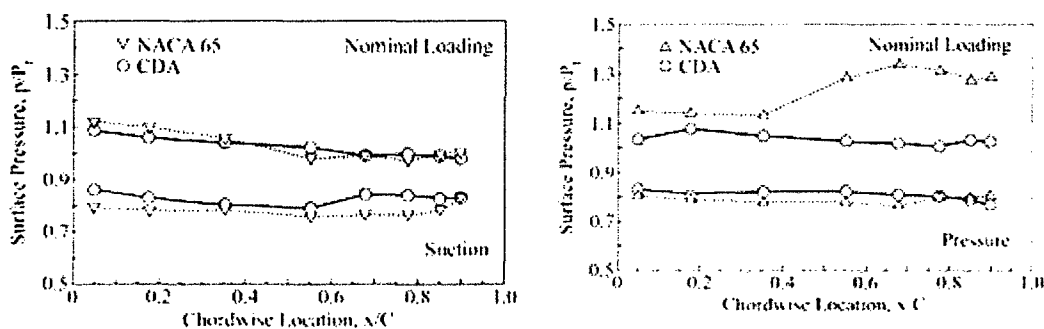


Figure 9. IGV unsteady surface pressure envelopes, nominal loading

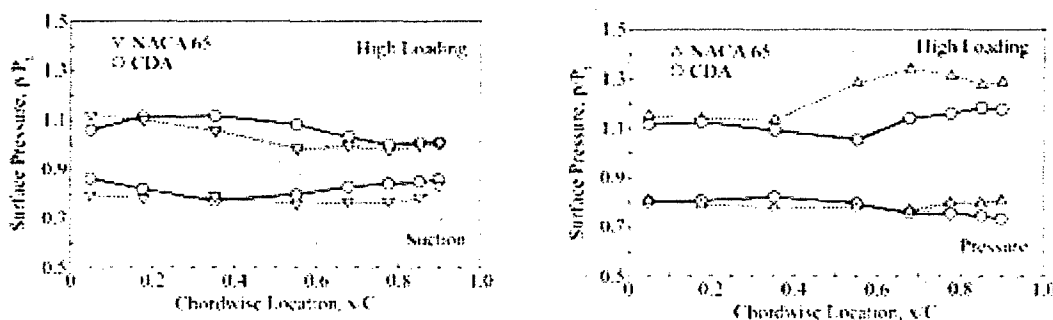


Figure 10. IGV unsteady surface pressure envelopes, high loading

On the pressure surface, the maximum unsteady pressure is highest along the aft 30% chord at high loading and almost uniform at nominal loading. The unsteady pressure on the pressure surface is significantly higher at the high than at nominal loading, although in both cases there is a reduction in unsteadiness as compared to with the NACA 65 rotor.

The suction surface unsteady pressure envelopes exhibit the opposite trend, with the unsteady loading highest forward of mid-chord, with nearly constant magnitude envelopes over the aft 30% of the IGV. The unsteadiness is highest at high loading, and lowest at nominal loading. On the suction surface, the response to both the CDA and NACA 65 generated forcing function are of similar magnitude.

The history of the phase-lock averaged pressure distributions at several time instances within one IGV-rotor interaction cycle are presented for the nominal and high loading in Figures 11 and 12. These instantaneous surface pressures are presented along with the rotor generated unsteady static pressure field. Careful inspection of these figures shows an essentially 1st harmonic response in the vane leading edge region, and a twice-per-cycle oscillation aft of mid-chord. This phenomenon is most evident at the high loading operating condition.

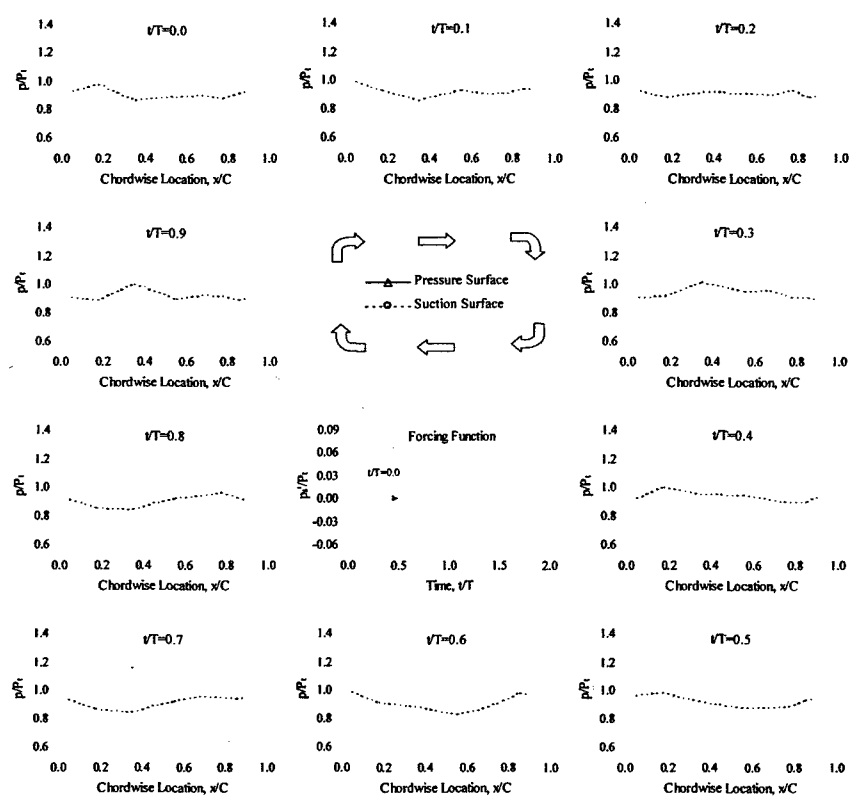


Figure 11. Instantaneous IGV pressure distributions, nominal loading

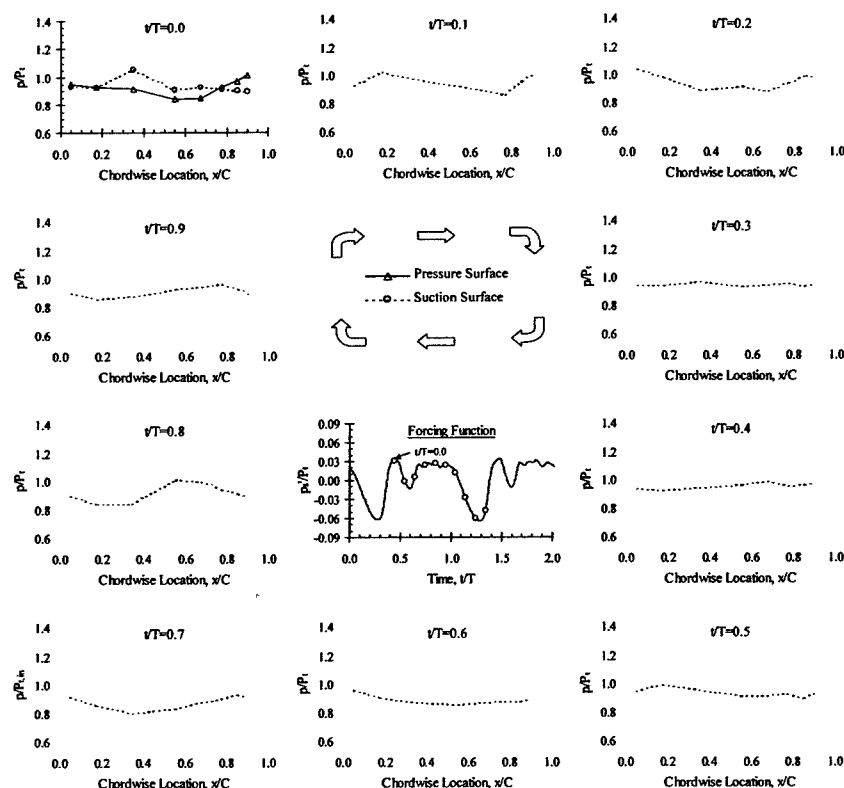


Figure 12. Instantaneous IGV pressure distributions, high loading

Rotor Wake Variability

As design trends for modern compressors result in increased blade row aerodynamic interactions, classic simplified views of forcing functions may no longer be sufficient to allow accurate predictions of blade response. Although CFD analysis holds promise, there are several key issues that are impeding progress towards a better predictive capability for compressor forcing functions that drive HCF. First, detailed data with which to calibrate these tools are lacking. Specifically, detailed full flow field data in test facilities where a realistic rotating machinery environment is achieved are required. Second, a better understanding of both the physical processes that dominate blade-row interactions as well as the limitations of standard modeling assumptions is required.

To address these issues, this effort investigated the validity of the “average rotor wake” forcing function. The aim of this research is to describe rotor wake variability using PIV. Previously acquired hot-wire data indicated significant rotor wake variability at mid-span. PIV allows identification of structures in the instantaneous flow field that contribute to this variability.

Statistical Wake Analysis

Hot-film measurements of the rotor allow the resolving of 2 components of the unsteady velocity that characterize the wake passage event. These mid-span data represent an ensemble average of 500 entire rotor revolutions; i.e. the average wake characteristics for each blade are preserved. Figure 13 presents the absolute flow angle of the rotor wakes at nominal steady loading, showing variations in downstream vane incidence angle induced by these wake fluctuations that range from -21.2° to $+1.8^\circ$ over one rotor revolution. The maximum incidence angle to the vanes differs by 1.8° over one complete rotor revolution. Also shown is the absolute flow angle of the rotor wakes at the low steady loading condition which is a typical off-design condition. The corresponding variations in vane incidence angle induced by the wake fluctuations at off-design range from -29.6° to $+2.1^\circ$ over one rotor revolution. The maximum incidence angle to the downstream stator vanes differs by as much as 13.0° over one complete rotor revolution.

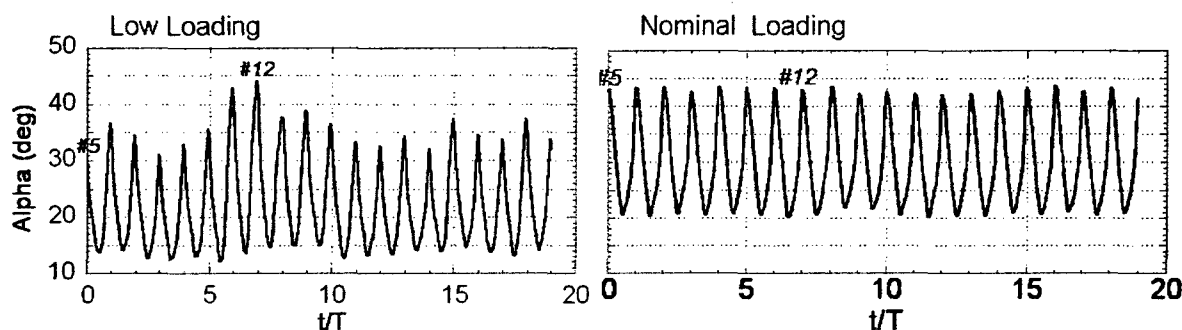


Figure 13. Ensemble-averaged wake absolute flow angle- nominal & low loading

The wake variability is also very significant with respect to the absolute Mach number, Figure 14. The rotor wake deficits range from 5.8% to 15.9% of the stator inlet Mach number over one rotor revolution. Since the highest variability occurs at the low steady loading condition at 100% speed, this operating point is the focus of this investigation.

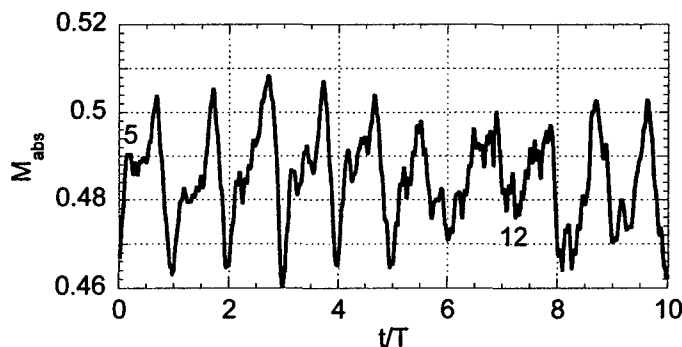


Figure 14. Ensemble-averaged rotor wake absolute Mach number at low loading

In harmonic analyses, each ensemble-averaged wake is assumed to be identical. However, as shown, some wakes are actually quite different. This means that the frequency content that describes the average wake is insufficient to describe the actual wake forcing function. Blade-to-blade variations introduce frequency content lower than blade pass event, as

well as changing the distribution of energy in the harmonics. Variability analysis is used to quantify these differences between wakes and determine the significance of this variability.

With a statistical significance level of 0.05, variability is not simply random. Thus, both the average and instantaneous structure of the wakes were measured using PIV to investigate the physical nature of the variability. Also, the wake of rotor Blade 12 is very different from the other wakes whereas that from Blade 5 is quite typical. Thus, a comparison of both the average and instantaneous wake structure of Blade 5 and Blade 12 is performed.

PIV Data

To investigate the large variability between Blades 5 and 12, PIV data are taken downstream of the rotor as the wakes convect into the stator passage. Figure 15 shows the axial Mach number data for the ensemble-averaged stator flow field when each blade is at $t/T = 1.0$ within its blade pass period. This corresponds to the case when the hot-film probe is in the center of the rotor wake. The axial Mach number deficit of the wake is plainly seen extending from the left lower corner, with the stator leading edge at the right. The Blade 12 wake exhibits a somewhat larger axial Mach number deficit as the wake evolves when compared to Blade 5.

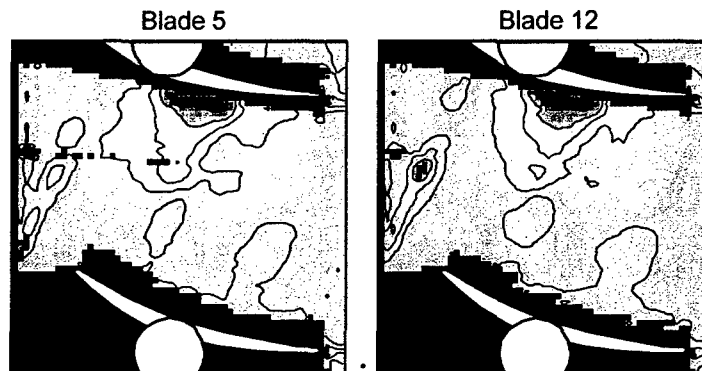


Figure 15. Ensemble Averaged M_{axial}

Figure 16 shows additional mid-span ensemble averaged data, with the imaging region focused on the emerging rotor wake. In the lower right portion of these figures, the stator leading edge appears in the image. The axial Mach number results clearly show that the wake from Blade 12 spreads more rapidly than that from Blade 5 as it convects towards the stator.

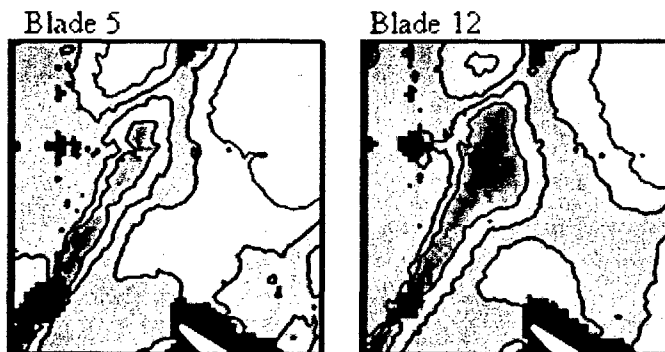


Figure 16. Ensemble Averaged M_{axial}

Figure 17 shows the mid-span vorticity field for Blades 5 and 12. The normal vorticity is calculated using a 2nd centered differencing requiring valid vectors on all sides of an interrogation region. Thus, more invalid regions are shown in the vorticity data than in the velocity data. The vorticity in the wake appears as a positive-negative pairing associated with counterclockwise and clockwise oriented fluid rotation in the structures that comprise the wake. The normal vorticity data give evidence that the Blade 12 wake is associated with structure. Emanating from the pressure side of the rotor blade, the Blade 12 wake positive vorticity region is much wider. In fact, the region of highest Blade 12 vorticity has shifted from the negative vortex strips of the wake and towards the leading edge of the stator. In general, the ensemble averaged wake of Blade 12 appears wider and less organized than that of Blade 5. It is rather difficult to extract structural information from the ensemble average, as the Strouhal shedding would be asynchronous with the blade motion and smeared by the averaging process.

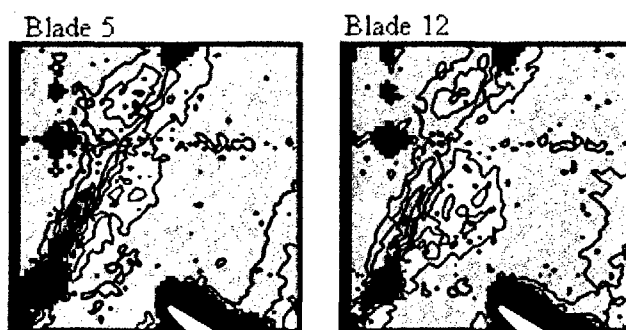


Figure 17. Ensemble Averaged Vorticity

Figure 18 provides insight into the reliability of the features observed in the ensemble averaged wake data. Presented is the standard deviation of the ensemble average for each separate interrogation region. There is a wider band of high standard deviation associated with the wake of rotor Blade 12. The magnified-image data show that in the same region where large positive vorticity was indicated for the Blade 12 wake, a region of high standard deviation agrees with that observed from the hot-film data. This provides evidence to support that an asynchronous shedding structure of significant scale could be responsible for the Blade 12 wake characteristics.

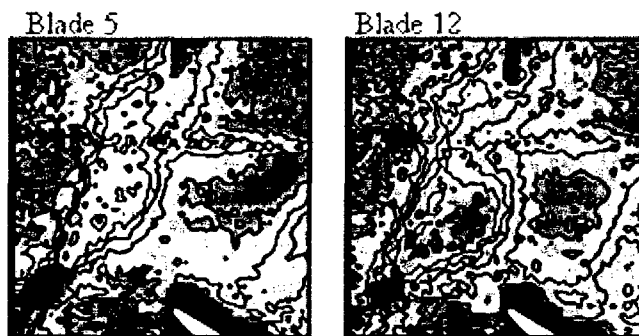


Figure 18. Standard Deviation in Ensemble Average of M_{axial}

To better quantify the differences between the wakes of Blade 5 and Blade 12, mid-span Mach number profiles are shown in Figure 19. The Blade 12 wake width is clearly larger than that of Blade 5. The maximum velocity deficit is nearly the same, however, the wake of Blade

12 has a larger velocity deficit near the pressure side. When considering the difference in minimum axial Mach number, that there is a minimal deficit difference between the two wakes indicates a difference in the absolute flow angle. Overall, the maximum wake deficit has decreased with downstream distance from the rotor trailing edge: a 27% reduction in velocity deficit exists when comparing the 47% chord profile to the 30% chord profile. It also appears that the wake of Blade 5 spreads with distance from the trailing edge. However, for Blade 12, the wake width appears constant with downstream location. The difference in the freestream velocity between the pressure and suction sides of the wake is also evident at the further axial locations, indicating the potential field effect of the stator.

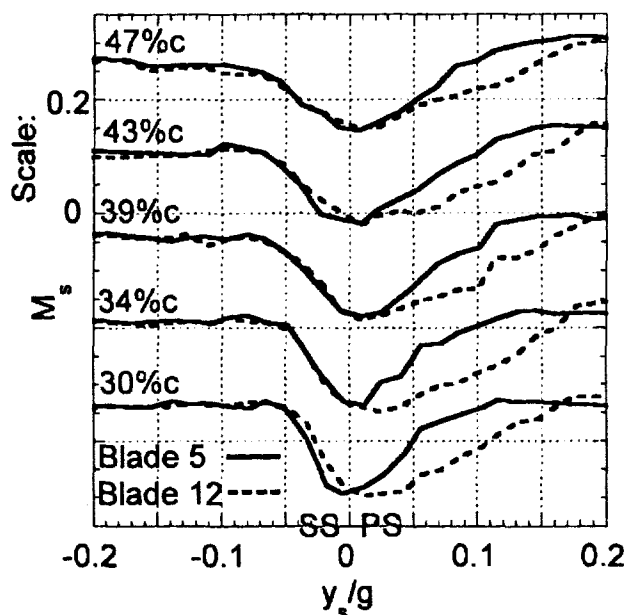


Figure 19. Wake profiles downstream of rotor trailing edge

To resolve some of the detailed physics of the variability in the ensemble averaged data, instantaneous data are also analyzed. Figure 20 shows the instantaneous axial Mach number for Blades 5 & 12. Three separate instantaneous images represent a single rotor relative position at $t/T = 1.0$. These figures demonstrate that while the variability between instances is obvious for each rotor blade, Blade 12 consistently appears to shed a wider wake than Blade 5. The Blade 12 wake shows more local regions of low axial velocity than that of the Blade 5 wake. These data deliver a portrait of the Blade 12 wake as being composed of larger-scale discrete structures which are shed asynchronously to the blade pass event. These structures are of large enough scale that they appear to have deviated from the straight-line convection path defined by the average wake centerline. Blade 5, however, seems to exhibit a well-defined wake characterized by smaller scale structures.

The structures shed from the pressure surface of Blade 12 have quite a different characteristic than those of Blade 5 or the suction surface of Blade 12. Normally, it is better to look at vorticity to identify structures in the flow field, but for the instantaneous images, the vorticity field proved to be less descriptive due to the high freestream turbulence. In the axial Mach number plots, these structures are more easily identified in the two lowest pictures in Figure 20 as the blue regions of low velocity. For Blade 5, they occur in evenly spaced pairs.

However, for Blade 12, the vortices shed from the pressure surface seem to be shed at a lower frequency than the other structures because of the larger spacing between vortex structures, be of larger extent, and feature the different convection path that would be typical of a large vortex structure. Such a structure would explain the high variability in this region seen in the standard deviation distributions. Since all data are taken at the same rotor relative position in front of the same stator vane, blade row interaction effects due to both the potential field and the IGV wake impinging onto the rotor row should be similar for both of these blades.

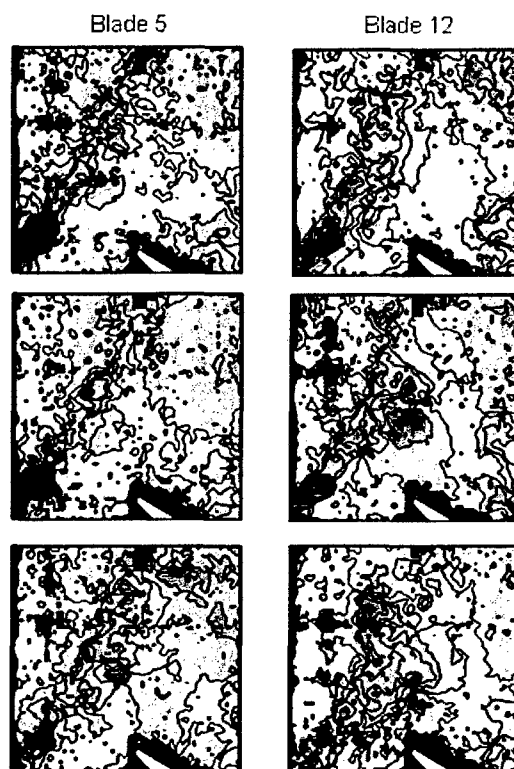


Figure 20. Instantaneous PIV images - M_{axial}

To confirm the uniformity of the approach flow, the instantaneous IGV flow field was examined for Blade 5 and Blade 12. No significant variations in the IGV flow field could be discerned between the two blades. Thus, there are no significant differences in the IGV flow fields at the instant corresponding to Blade 5 and Blade 12 at $t/T = 1.0$ that could be responsible for the significant variation in wake features. The similarity in the IGV flow fields indicates that both rotor blades are experiencing similar potential field effects at this location.

Figures 21 and 22 show axial Mach number and normal vorticity for the ensemble-averaged stator flow field at 90% span. As at mid-span, no discernable differences are noticed in the IGV flow field data that would suggest variation upstream of the rotor. In general, it is observed that the structure revealed by the ensemble averaged data is far more complex and less well structured than that at mid-span. A large accumulation of low momentum fluid is along the stator pressure surface and spreads across the passage towards the suction side. This region is likely the result of the wake fluid convecting up along the pressure surface and will complete the circulation pattern by moving towards the suction surface in the endwall boundary layer.

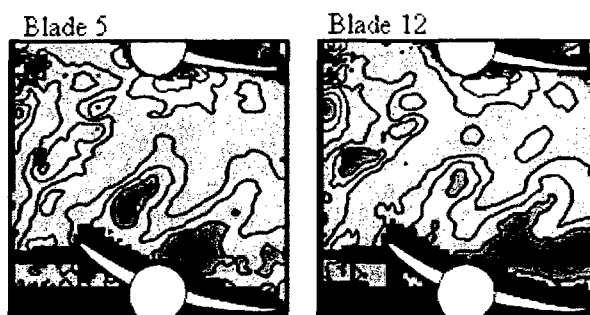


Figure 21. Ensemble-averaged M_{axial} in stator passage at 90% span

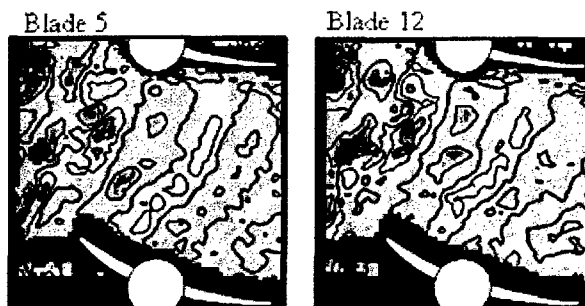


Figure 21: Ensemble-averaged vorticity at 90% span

The vorticity data show a generally broader wake structure, with the wakes at 90% span sloped more towards axial than those at 50% span. This is consistent with the blockage associated with the low momentum wake fluid that has accumulated on the stator pressure surface.

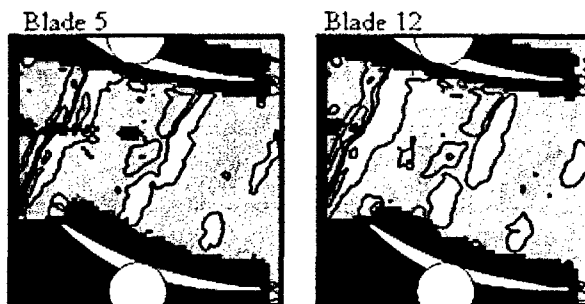


Figure 22. Ensemble-averaged vorticity at mid-span

The differences between the ensemble-averaged wakes for Blade 5 and Blade 12 at 90% span are not as obvious as the differences at 50% span. However, small differences would be somewhat masked by the number of features in the flow field. In the mid-span data, the standard deviation in axial Mach number was the most reliable indicator of the variability in the Blade 12 wake. This is not as easily seen, however, at 90% span, Figure 23. The tip data exhibit larger overall standard deviation throughout the ensemble averaged flow field as expected because of the unsteady interactions with tip clearance vortices and secondary flows which are asynchronous to the blade pass period. A careful consideration of the 90% span data fails to identify any distinct differences in wake widths as were seen at mid-span. If the tip region

variations were the "source" of the variability, it is likely that they would be larger than those observed at mid-span and thus more apparent.

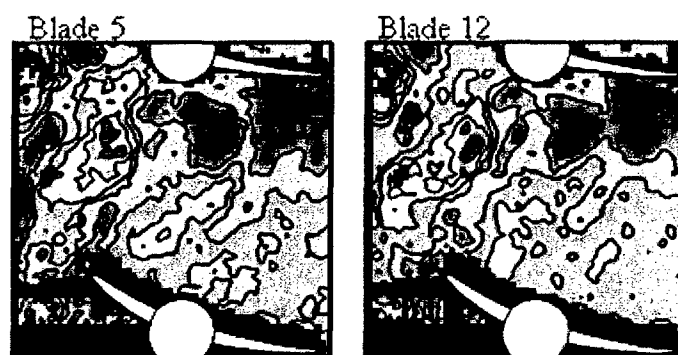


Figure 23. Standard deviation of ensemble-averaged M_{axial} field at 90% span

The geometry of Blades 5 and 12 were measured and compared with the other blades to determine if this was a contributor to the variability. The trailing edge thicknesses of Blade 5 and Blade 12 differ by 0.003 in., which is within the maximum 0.005 in variation measured for all of the rotor blades. Also, the variation in mid-span stagger angle between the two blades was measured to be no more than one degree, and there was not an observable change in rotor shock angle when investigating the IGV flow field at 90% span. These geometrical differences due to manufacturing capabilities are typical of modern compressors.

A difference between Blade 5 and Blade 12 is in the rotor balance ring. The largest amount of mass has been removed from the balance ring on both sides of the rotor near Blade 12, effectively reducing the radial extent of what forms a simple planar seal. Although the disk cavity is fairly isolated from the surroundings, it is possible that the seal flows could be contributing to the observed wake variability, whereby flow could be emerging into the rotor flow field via a viscous or blade-potential driven pumping phenomenon. This could also explain why the larger variability is seen at the low steady loading condition. The lower pressure would set up a condition for a pressure-driven flow out of the seal and into the flowpath. Thus, the higher steady loading conditions would not provide the pressure gradient to allow the leakage flow to affect the wakes at mid-span. However, the rotor wake variability is insignificant toward the tip, and this supports the notion that the source of the variability could be near the hub.

ACKNOWLEDGEMENT/DISCLAIMER

This work was sponsored (in part) by the Air Force Office of Scientific Research, USAF, under grant/contract number F49620-97-009. The views and conclusions contained herein are those of the authors and should not be interpreted as necessarily representing the official policies or endorsements, either expressed or implied, of the Air Force Office of Scientific Research or the U.S. Government.

RESEARCH ASSISTANTS

John Papalia, Ph.D., Purdue University

Nicole Key, Ph.D. Candidate, Purdue University

PUBLICATIONS

"Rotor Blade-To-Blade Wake Variability and Its Effect on Downstream Vane Response," Sanders, A.J. and Fleeter, S., *AIAA Journal of Propulsion and Power*, Vol. 18, No. 2, March-April 2002, pp. 456-464.

"A PIV Investigation of Rotor-IGV Interactions in a Transonic Compressor," Sanders, A.J., Papalia, J. and Fleeter, S., *AIAA Journal of Propulsion and Power*, Vol. 18, No. 5, September-October 2002, pp. 969 – 977.

"Airfoil Row Wake Interactions in a High Speed Axial Compressor," Johnston, R.T. and Fleeter, S., *AIAA Journal of Propulsion and Power*, Vol. 18, No. 6, November-December 2002, pp. 1280 - 1288.

"Three-dimensional Time-Resolved Inlet Guide Vane-Rotor Rotor Potential Field Interaction," Johnston, R.T. and Fleeter, S., *AIAA Journal of Propulsion and Power*, Vol. 20, No. 1, 2004, pp. 171-180.

"Three Dimensional Wake Forcing Functions Generated by a High Speed Rotor," Johnston, R.T. and Fleeter, S., *AIAA Journal of Propulsion and Power*, Vol. 21, No. 1, January-February 2005, pp. 175-182.

Key, N. Lawless, P.B., and Fleeter, S., "Rotor Wake Variability in a Transonic Compressor Stage," *ASME Paper GT-2004-53486*, ASME Gas Turbine Conference, June 2004.

"CDA Rotor Generated Unsteady Aerodynamics of an Upstream Vane Row," J. Papalia, P.B. Lawless and S. Fleeter, *AIAA Paper 2003-4977*, July 2003

"Steady Loading Effects on Rotor-Stator Interactions in a Transonic 1½-Stage Compressor," J. Papalia, P.B. Lawless and S. Fleeter, *ISABE-2003-1128*, September 2003.

Key, N. Lawless, P.B., and Fleeter, S., "Rotor Wake Variability in a Transonic Compressor Stage," *ASME Paper GT-2004-53486*, ASME Gas Turbine Conference, June 2004.

"Rotor-Generated Unsteady Aerodynamic Interactions in a 1½ Stage Compressor," Papalia, John, J., *Purdue University Ph.D. Thesis*, December 2004.